MODELING AND CHARACTERIZATION OF MICROSTRUCTURE EVOLUTION IN SINGLE-CRYSTAL SUPERALLOYS PROCESSED THROUGH SCANNING LASER EPITAXY

Amrita Basak*, Ranadip Acharya*, and Suman Das*

* George W. Woodruff School of Mechanical Engineering, Georgia Institute of Technology, Atlanta, GA 30332

Abstract

This paper focuses on microstructure evolution in single-crystal alloys processed through scanning laser epitaxy (SLE); a metal powder-bed based additive manufacturing technology aimed at the creation of equiaxed, directionally-solidified or single-crystal structures in nickel-base superalloys. Galvanometer-controlled movements of the laser and high-resolution raster scanning result in improved control over the melting and solidification processes in SLE. Characterization of microstructural evolution as a function of the complex process physics in SLE is essential for process development, control and optimization. In this paper an ANSYS CFX based transient flow-thermal model has been developed to simulate microstructure characteristics for single-crystal superalloys such as CMSX-4 and René N5. Geometrical parameters and melt pool properties are used to estimate the resulting solidification microstructure. Microstructural predictions are compared to experimental metallography and reasonably good agreement is achieved. This work is sponsored by the Office of Naval Research through grants N00014-11-1-0670 and N00014-14-1-0658.

Introduction

The ever increasing demand for operating the gas-turbine engines at higher pressure and temperature has increased the inlet temperature of the hot-section components. The hot-section components used for aircraft propulsion and industrial power generation represent one the most aggressive applications of high temperature materials. Single-crystal (SX) technology is widely used today in modern gas-turbine aero-engines and land-based power generation systems as the SX microstructure prevents grain boundary sliding, thus causing enhanced creep strength and thereby improving the power and thermal efficiency significantly. The single-crystal blades are typically produced by investment casting in a directional solidification furnace by placing a grain selector or a seed of desired crystallographic orientation at the bottom of the mold to achieve the required single-crystal orientation. However over a period of time, these rotating turbine blades undergo thermal corrosion, high temperature oxidation; and suffer from tip material loss. Currently, lack of any suitable commercial repair technologies results in high maintenance costs for these components as once they lose certain amount of tip-material, they have to be scrapped. Hence, it is of great interest to develop an additive manufacturing (AM) technology that can restore the single-crystal microstructure at the damage locations so that the blades can be put back to service. This paper focuses on computational process development for scanning laser epitaxy (SLE); a laser-based additive manufacturing process that has demonstrated the capability to repair these high-value components.

SLE is a metal powder-bed based fusion-based additive manufacturing technology that has been demonstrated to create equiaxed (EQ), directionally solidified (DS) and single-crystal (SX) structures of nickel superalloys onto similar-chemistry substrates through controlled melting and re-solidification of superalloy powders and substrates. In SLE, a galvanometer controlled high power laser beam is directed onto the powder bed. Laser power, preheat, scan speed and scan spacing are varied to control the optimal energy density that ensures a good metallurgical bond between the substrate and the powder; and generates a desired SLE deposit. The metallurgical bond starts at one edge of the substrate where the preheat scans initiate a melt pool. The melt pool then travels along the length of the substrate fusing the powder to the substrate. Under the proper operating conditions and with sufficient substrate melt-back, the solidification microstructure has been demonstrated to mimic the morphology of the underlying substrate, allowing for single-crystal growth.

Computational modeling of the complex SLE process can provide significant insights in understanding the fundamental physics of the problem. Several reports on the simulation of laser based additive manufacturing approaches can be found in literature. Both Finite Element Methods (FEM) and Finite Volume Methods (FVM) are used for the thermal modeling of the system [1, 2]. Gaumann coupled the columnar-to-equiaxed-transition (CET) modeling with the Rosenthal solution [3]. Rappaz et. al. provided a detailed modeling of the microstructure and columnar orientation based on the solidification velocity and crystalline orientation [4]. This approach is based on the selection of the growth direction that closely follows the melt pool normal direction. Later on, substrate orientation is also taken into account [5, 6]. Acharya et al. [7] has developed a three-dimensional CFX-based CFD model and obtained good qualitative agreement with the experimental CET data for CMSX-4 processed through SLE.

In this work, an ANSYS CFX based two-dimensional frame work has been developed to simulate and compare the melt pool for different single-crystal superalloys. The two-dimensional model reduces the computational time by approximately 70% compared to the three-dimensional model, and is proved to be efficient during the SLE screening trials. The movement of the laser beam along the x and y directions is modeled as a line source scanning in the x-direction. The laser power profile in the y-direction is modeled from the transient averaged data for a single scan and approximated with a 10th degree polynomial [8]. This polynomial is found to be flat in the middle region with some reduction of intensity near the edges of the sample. This characteristic of the power profile justifies the simplification of the computationally expensive three-dimensional CFD model to a computationally tractable two-dimensional simulation. The width of the coupon is used to calculate the residence time of the line heat source at any given position, and then the heat source is advanced in the forward direction by the scan spacing. The complete scan pattern is formulated using ANSYS CFX user-defined functions. The heat conduction equation is used to model the transfer of heat to the base plate. The associated melting and re-solidification of the powder and the substrate is formulated by the equilibrium phase change model. Heat transfer to the base plate is modeled using the heat conduction equation. Analysis of the flow-field modeling reveals the formation of rotational vortices due to the moving heat source and Boussinesq convection. The transient melt pool information is used to predict the oriented-to-misoriented-transition (OMT) and columnar-to-equiaxed-transition (CET). The simulation and the post-processing are performed in the ANSYS CFX modeling environment that allows the integration of the thermal modeling with the microstructure

prediction. Reasonable qualitative agreement between the simulation and the experimental results is achieved.

SLE Experimental Procedure

The nickel-base superalloys such as CMSX-4 and René N5 are chosen in this work. The powders are produced by Praxair Surface Technologies using an atomization process. Table 1 summarizes the chemical composition of these superalloy powders.

Table 1. Chemical composition of various superalloys (wt. %)

	Cr	Co	Mo	Re	W	Al	Ti	Ta	Hf	B	C	Zr	Ni
CMSX-4	6.5	9.7	0.4	3.0	6.4	5.6	1.0	6.5	-	-	-	-	Bal
René N5	7.1	8.0	2.0	3.0	5.0	6.0	-	7.0	-	-	-	-	Bal

The SLE process is conducted on rectangular SX cast CMSX-4 and René N5 coupons having dimensions of 35.56mm X 6.86mm X 2.54mm. Each substrate coupon is placed into a 35.56mm X 6.86mm recess cut into an Inconel 625 base plate. The powder is placed above the substrate using rectangular wells cut into an Aluminum mask plate. Once the samples are prepared, they are placed into an atmospheric process chamber that is purged with high purity (99.999%) Argon. A 1kW Ytterbium fiber laser (IPG Photonics, Model: YLS-1000) is used with a Cambridge Technologies galvanometer scanner to focus the beam on top of the powder bed. A raster scan pattern across the width of the sample generates a melt pool that linearly propagates along the length of the substrate. The details of the experimental setup can be found elsewhere [8], and is skipped here for brevity.

SLE Deposit Characterization

SLE processed samples are sectioned along the length and width for the inspection of the microstructure. A Buehler automated saw is used to cut the samples. A Leica DM6000 optical microscope is thereafter used to take the images. Figure 1 demonstrates length wise cross-sectional view of crack-free CMSX-4 sample as processed by SLE showing a full metallurgical bond along the entire length of the sample. The metallurgical bond starts on the left side of the image where the melt pool is generated by the preheat scans.

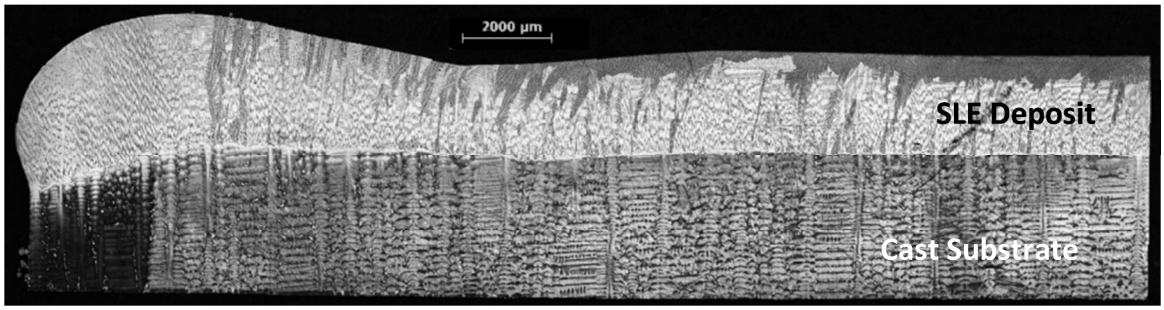

Figure 1. Representative lengthwise section of the first half of a CMSX-4 sample with the starting edge on the left side of the image.

Figure 2 provides a similar cross-sectional image of another single-crystal alloy i.e. René N5. There is an excellent metallurgical bond between the substrate and the deposit region that is crack-free and dense.

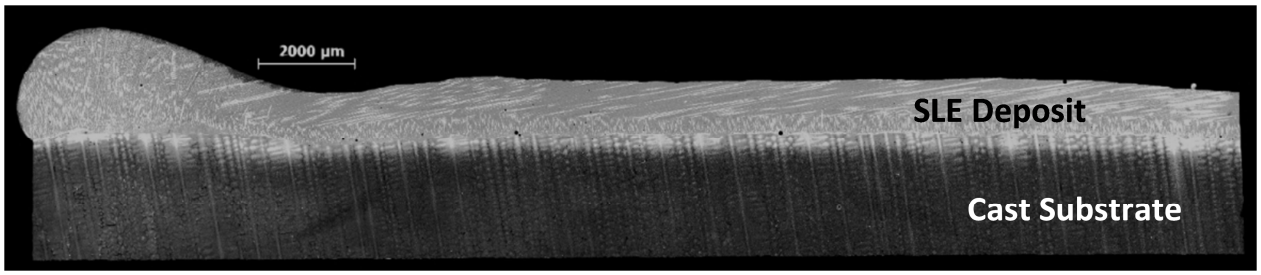

Figure 2. Representative lengthwise section of the first half of a René N5 sample with the starting edge on the left side of the image.

Computational Flow-Thermal Modeling of SLE

A transient, multi-domain model with temperature dependent thermos-physical property values is used to simulate the flow-thermal behavior of the SLE to predict the melt pool characteristics. Temperature dependent property data for CMSX-4 and René N5 is modeled using tabular data [9, 10, and 11]. The pseudo-2D model includes two separate domains – (1) the deposit domain consisting of the substrate and the powder and (2) the Inconel baseplate domain. Figure 3 shows the geometry and mesh for the 2D configuration. The deposit domain has a finer mesh to accurately capture the 20 micron radius laser heat source. The total node count of the mesh is close to 137k and the skewness is below 0.2. The simulation is performed in ANSYS CFX solver.

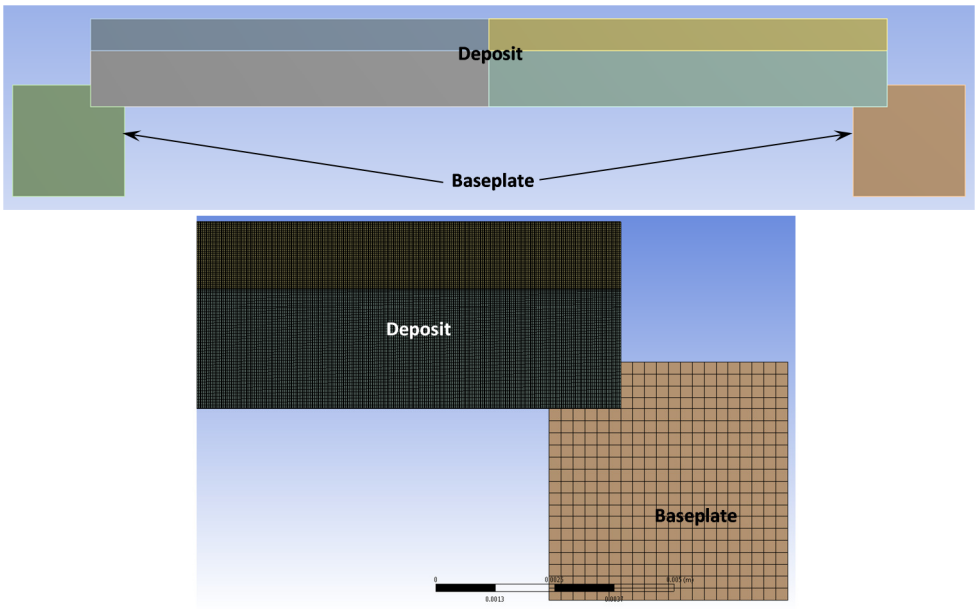

Figure 3. ANSYS CFX simulation model showing different domains – Deposit domain and Baseplate domain.

The solid and liquid component enthalpy equations, expressed in terms of volume fraction, r, are:

$$\frac{\partial(\rho_S r_S h_S)}{\partial t} + \nabla \bullet (\rho_S r_S \underline{U}_S h_S) = \nabla \bullet (r_S k_S \nabla T_S) + I \tag{1a}$$

$$\frac{\partial(\rho_L r_L h_L)}{\partial t} + \nabla \bullet (\rho_L r_L \underline{U}_L h_L) = \nabla \bullet (r_L k_L \nabla T_L) - I \tag{1b}$$

Here ρ is the density, h is the enthalpy (including the latent heat), T is the temperature, U is the velocity and I is the interphase heat transfer. The subscripts S and L refer to the solid and liquid components respectively. Equations (1a) and (1b) can also be expressed more compactly.

$$\frac{\partial(\overline{\rho} h)}{\partial t} + \nabla \bullet (\overline{\rho} \underline{U} h) = \nabla \bullet (\overline{k} \nabla T) - \nabla \bullet (\overline{\rho} Y_S (\underline{U} - \underline{U}_S)(h_L - h_S)) + S \tag{2}$$

Here $\overline{\rho}$ is mixture density, h is the mixture enthalpy, $\overline{k}$ is mixture conductivity, Y_S is the mass fraction of solid [12]. The final term of Equation (2) represents an additional source due to the difference in velocity between the solid and liquid components. This term has a finite value in the mushy region of the flow ($0< Y_S, Y_L <1$). In the regions of pure liquid or pure solid, the mixture enthalpy equation reduces to the appropriate component enthalpy equation. The volume fractions of liquid and solid component are incorporated using tabular data representing solid and liquid fraction of the superalloys in the melting range. The Boussinesq approximation is implemented to model the effect of variable liquid density.

A Darcy like source term is incorporated to model the resistance to flow in the mushy region. The permeability is modelled using Kozeny-Carman equation [13]. To prevent division by zero, the term is bounded by a user-specified maximum, C.

$$\underline{S}_M = \min\left(C, \frac{\mu_L}{K_0} \frac{(1 - r_L)^2}{r_L^3}\right)(\underline{U} - \underline{U}_S) \tag{3}$$

In the turbulence equations, sink terms similar to the Darcy term in the momentum equation are applied to damp the turbulence in solid regions [12].

$$S_k = -\frac{\mu_L}{K_0} \frac{(1 - f_L)^2}{f_L^3} k \quad , \quad S_\varepsilon = -\frac{\mu_L}{K_0} \frac{(1 - f_L)^2}{f_L^3} \varepsilon \tag{4}$$

For the baseplate domain, the conduction heat equation is solved.

$$\frac{\partial(\rho H)}{\partial t} = \nabla.(K \nabla T) + S_0 \tag{5}$$

Here ρ is the density, H is the enthalpy, K is the thermal conductivity and S_0 is the source/sink term.

The conservation of thermal energy is achieved at all interfaces. The convection heat loss is modeled as a surface sink term using Newton's law of cooling. Radiation loss is modeled using a sink term. The transient model is solved using a time-step value approximately equal to 0.002 s. The inclusion of convection, phase change model and Darcy sink term requires a smaller time-step value for solver stability. The convergence is assured once the RMS value of residual is reduced below 10e-4. Once solved, the result is post-processed in CFD-post to analyze the melt pool nature, the melt depth profile and the temperature distribution.

Results and Discussion

Computational simulation of the SLE process throws light on the nature of the flow-thermal field generated by the moving heat source as it travels along the length of the substrate. The flow field affects the melt pool formation and the temperature distribution within the melt pool. Figures 4(a) and 4(b) show the temperature distribution and the velocity vectors superimposed on the temperature field inside the CMSX-4 melt pool. The melt pool is identified in the regions with liquid CMSX-4 mass fraction of 0.99 or more. This calculation is validated by the fact that inside the melt pool, the temperature is greater than 1654K, the liquidus temperature of CMSX-4. The melt pool consists of two counter rotating vortices with their center located approximately at the location of the laser heat source.

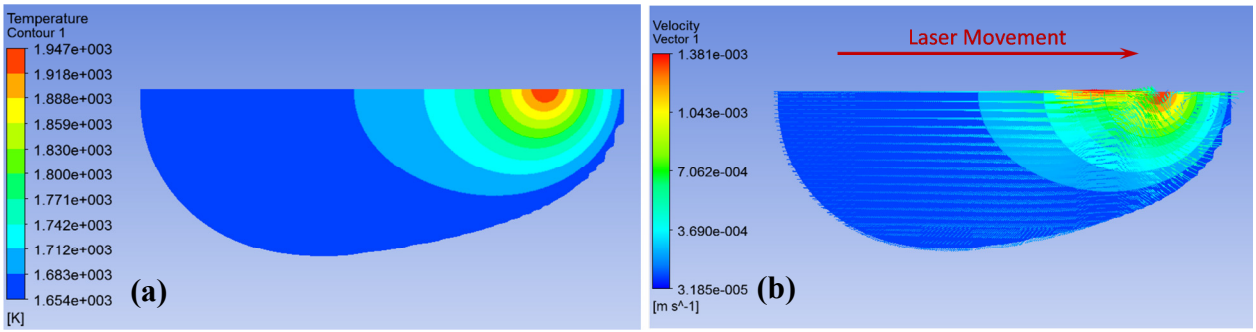

Figure 4. (a) Contour of velocity, (b) Contour of temperature inside the melt pool for CMSX-4.

Characterization of SLE Melt Depth

The melt depth profile is of immense interest for the present application as it characterizes quality of the metallurgical bond between the powder and the substrate. The melt depth is obtained from the CFD simulation, and compared with the actual cross-sectional optical micrographs. Figure 5(a) and 5(b) demonstrate the melt depth comparison between simulation and experimental results for CMSX-4 and René N5 respectively. A good agreement is obtained between simulation and experiment results for different single-crystal superalloys.

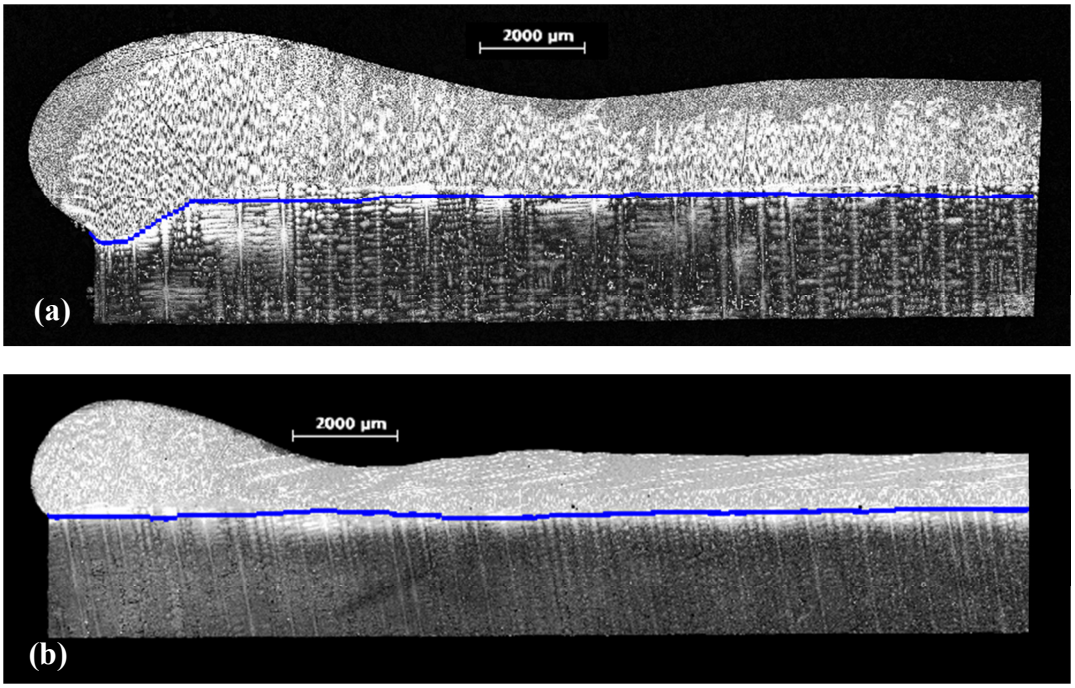

Figure 5. Comparison of the simulated melt depth (blue line) with actual micrograph for (a) CMSX-4, (b) René N5.

Microstructure Modeling

Modeling of solidification microstructure is carried out to understand the following phenomena of single-crystal superalloys – (a) oriented-to-misoriented-transition (OMT) and (b) columnar-to-equiaxed-transition (CET).

(a) Oriented-to-misoriented-transition (OMT) Modeling: In order to characterize the columnar orientation, inner product of the normal component of the solid-liquid interface with the (100) and (001) direction vectors is resolved. Here the direction vectors represent the possible dendrite orientations. The maximum value of the inner product provides the minimum of the cosine component of the inclination angle between the two directions. Hence,

$$\cos\psi = \max\left(\hat{\mathrm{n}}.\hat{u}\right) \tag{6}$$

Here, $\hat{\mathrm{n}}$ is the normal vector to the solid-liquid interface and $\hat{u}$ is the direction vector. The orientation vectors for (001) and (100) are assigned values of 1 and 100 respectively. The plot of the orientation vector is shown in Figs. 6(a) and 6(b) for CMSX-4 and René N5 respectively for a given position of the laser heat-source. The flip in direction from (001) to (100) is suggested in the plot as evidenced in the lengthwise metallographic images of the samples. The two-dimensional simulation cannot capture the flip along the y-direction (010). The trailing edge flip location is calculated for CMSX-4 and René N5; and is indicated by the yellow line. The melt-back depth is indicated by the green line while the instantaneous laser heat-source is denoted by the purple plane. The flip height for CMSX-4 is higher compared to René N5 that can be seen in the lengthwise metallographic images of the samples.

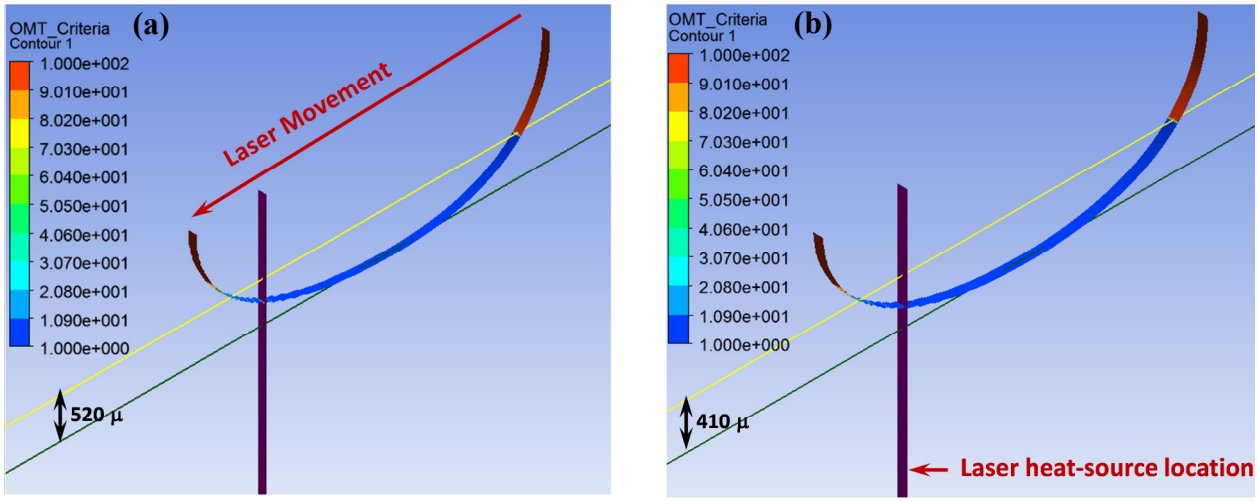

Figure 6. Orientation vector plot showing OMT for (a) CMSX-4 and (b) René N5 on the solid-liquid interface.

(b) Columnar-to-equiaxed-transition (CET) Modeling: The temperature gradient at the solid–liquid interface (G) is computed from the ANSYS CFD model. The solid–liquid interface orientation (θ_i) is calculated from the following expression:

$$\theta_i = \cos^{-1} (G_i/G) \text{ (For i = x, y, z)} \quad (7)$$

The growth rate of the solid–liquid interface is given by V = S cos θ (S = Scan speed). The angle ψ refers to the angle between the normal vector and the possible dendrite growth orientation at the solid–liquid interface, and is evaluated in CFX-Post. The temperature gradient parallel to the dendrite growth direction is calculated using the equation, $G_{hkl} = G/\cos \psi$. The dendrite growth velocity, V_{hkl}, is calculated using the equation $V_{hkl} = S \cos\theta / \cos \psi$. The Rappaz modification [7] is applied to predict the CET as follows:

$$\frac{G_{hkl}^{n}}{V_{hkl}} \geq a\left[3\sqrt{\frac{-4\pi}{3\ln(1-\phi)}}\sqrt{\frac{N_0}{n+1}}\left(1-\frac{\Delta T_n^{n+1}}{\Delta T_{tip}^{n+1}}\right)\right]^{n} \quad (8)$$

Here a, n = material constant [7, 14], φ = equiaxed fraction (critical value = 0.066 %), N_0 = nucleation density, ΔT_{tip} = tip undercooling, and ΔT_n = nucleation undercooling.

Figure 7(a) and 7(b) show the temperature gradient contour for CMSX-4 and René N5 for a given position of the laser heat-source denoted by the green surface. The laser heat-source movement direction is marked by the red arrow in Fig. 7(a). The leading edge shows a temperature gradient that is much higher compared to the trailing edge (Approximately 150 times higher). This elevated temperature gradient at the leading edge reduces the surface tension coefficient significantly, resulting in Marangoni convection. Any change in temperature at the leading edge may affect the way loose powder is drawn towards the melt pool resulting in waviness in the deposit height.

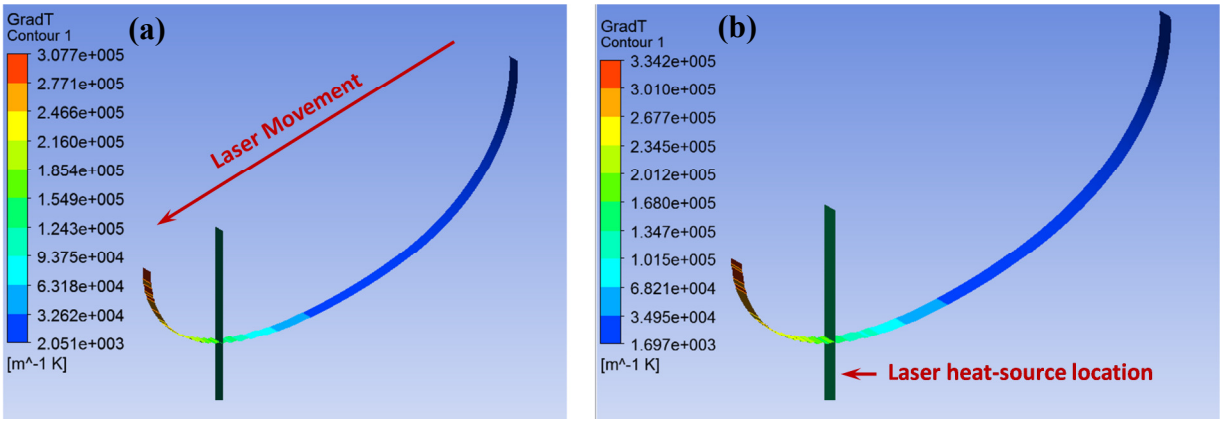

Figure 7. Temperature gradient at the solid-liquid interface (a) CMSX-4, (b) René N5. The green surface shows the instantaneous laser-heat source position.

Figure 8(a) and 8(b) show the plot of the G^{n}_{hkl}/V_{hkl} ratio for CMSX-4 and René N5 at the same laser-heat source position. Figure 8(b) shows a lower value of G^{n}_{hkl}/V_{hkl} ratio. Hence, the model suggests a lower columnar height in Figure 8(b) that can be verified from the metallographic images as observed in Figs. 9(a) and 9(b).

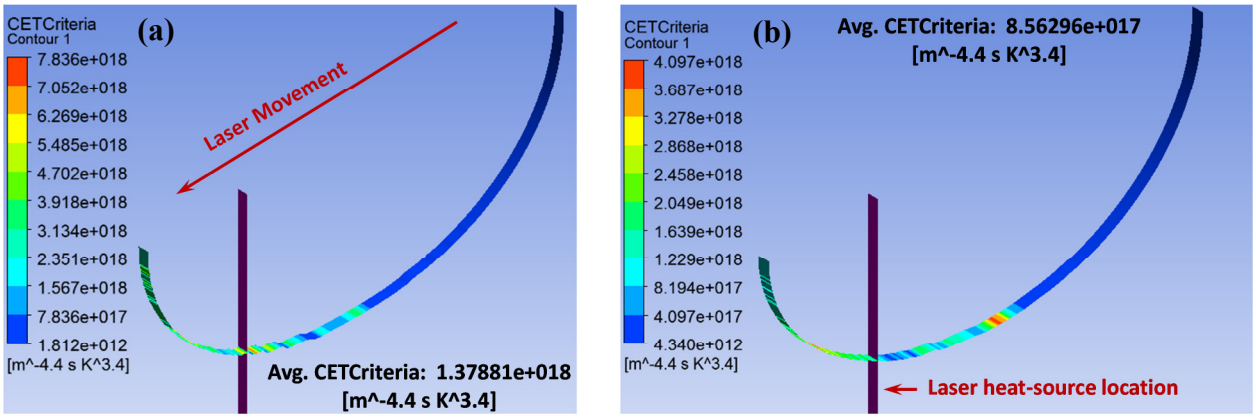

Figure 8. CET criterion plot for (a) CMSX-4 and (b) René N5 at laser heat-source position of 10.00 mm.

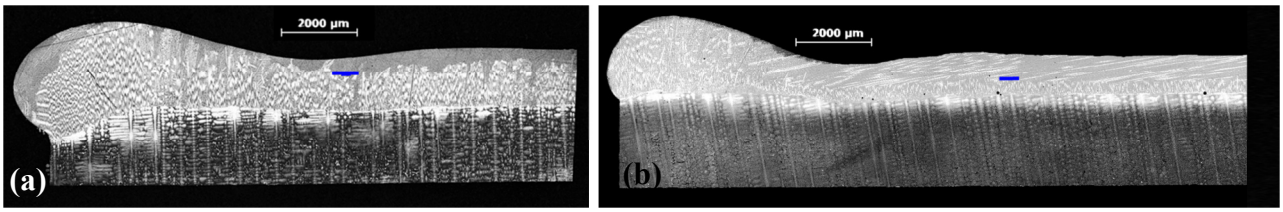

Figure 9. Experimental micrograph showing CET (indicated by blue line) for (a) CMSX-4 and (b) René N5 at laser heat-source position of 10.00 mm.

Conclusions

In the current work, a two dimensional CFD-based modeling scheme is developed to simulate the SLE process. The model is able to predict the melt pool behavior for various single-crystal superalloys. Excellent agreement has been obtained for the melt depth between the simulation and the experimental results. The same platform also includes the modeling of solidification microstructure to predict the OMT and the CET. The simulation estimates the possibility of CET, and shows reasonable qualitative agreement with the experimental data in predicting the CET. However, determination of the CET criterion from experimental studies is necessary to obtain quantitative data for microstructural investigation e.g. columnar to equiaxed ratio. The final aim is to develop a SLE processing map based on the CET criteria that will allow prediction of the microstructure beforehand.

Acknowledgments

This work is sponsored by the Office of Naval Research through grants N00014-11-1-0670 and N00014-14-1-0658.

References

1. T. D. Anderson, J. N. DuPont, and T. DebRoy, "Origin of stray grain formation in single-crystal superalloy weld pools from heat transfer and fluid flow modeling," Acta Materialia, vol. 55, pp. 1441-1454, 2010.
2. T. H. C. Childs, C. Hauser, and M. Badrossamay, "Mapping and Modelling Single Scan Track Formation in Direct Metal Selective Laser Melting," CIRP Annals - Manufacturing Technology, vol. 53, pp. 191-194, 2004.
3. M. Gaumann, "Epitaxial Laser Metal Forming of a Single Crystal Superalloy" (Ph.D. Thesis, EPFL Lausanne, 1999).
4. M. Rappaz and C. A. Gandin, "Probabilistic modelling of microstructure formation in solidification processes," Acta Metallurgica et Materialia, vol. 41, pp. 345-360, 1993.
5. S. Mokadem, C. Bezençon, A. Hauert, A. Jacot, and W. Kurz, "Laser Repair of Superalloy Single Crystals with Varying Substrate Orientations," Metallurgical and Materials Transactions A, vol. 38, pp. 1500-1510, 2007.
6. W. Liu and J. N. DuPont, "Effects of substrate crystallographic orientations on crystal growth and microstructure development in laser surface-melted superalloy single crystals. Mathematical modeling of single-crystal growth in a melt pool (Part II)," Acta Materialia, vol. 53, pp. 1545-1558, 2005.
7. Acharya, R., et al., “A comprehensive thermal, fluid flow and solidification model for the processing of single-crystal alloy CMSX-4 through scanning laser epitaxy for turbine engine hot-section component repair (part I),” Metallurgical and Materials Transactions B, vol. 45, pp. 2247-2261, 2014.
8. Acharya, R., et al. “Additive manufacturing of IN 100 superalloy through scanning laser epitaxy for turbine engine hot-section component repair: process development, modeling, microstructural characterization, and process control,” Metallurgical and Materials Transactions A, *to appear, 2015.*

9. T. Matsushita, H.-J. r. Fecht, R. K. Wunderlich, I. Egry, and S. Seetharaman, "Studies of the Thermophysical Properties of Commercial CMSX-4 Alloy," J. Chem. Eng. Data, vol. 54, pp. 2584-2592, 2011.
10. P.K. Sung, D.R. Poirier, and S.D. Felicelli Quested, "Simulating the Initiation of a Channel during Directional Solidification a Superalloy," Metallurgical and Materials Transactions A, vol. 32A, pp. 203-207, 2001.
11. D. Giuranno, S. Amore, R. Novakovic, and E. Ricci, "Surface tension and density of RENE N5® and RENE 90® Ni-based superalloys," Journal of Materials Science, vol. 50, pp. 3763-3771, 2015.
12. I. Hamill, "Implementation of a Solidification Model in CFX-5," CFX Ltd.2003.
13. W. L. S. McCabe, C. Julian, and P. Harriot, "Unit Operations of Chemical Engineering," 7 ed. New York: McGraw-Hill, 2005.
14. J. Vitek, S. David, and S. Babu, "Welding and Weld Repair of Single Crystal Gas Turbine Alloys," EPRI-RRAC Fifth International Conference on Welding and Repair Technology for Power Plants, June 26-28, 2002, Point Clear, Alabama.